ChemComm

COMMUNICATION

View Article Online
View Journal | View Issue

Check for updates

Cite this: *Chem. Commun.*, 2024, **60**, 13055

Received 19th August 2024,
Accepted 2nd October 2024

DOI: 10.1039/d4cc04112g

rsc.li/chemcomm

Published on 10 October 2024. Downloaded on 2/13/2026 7:29:37 AM.

Fe_3O_4 nanostructure films as solar-thermal conversion materials for ammonia synthesis†

Rong Fu, *[ab] Di Lei,[a] Zhenlu Li,[b] Hangjian Zhang,[b] Xiaofei Zhao[c] and Shuo Tao [a]

Here, we report that black photothermal materials elevate solar heating temperatures across high solar absorption and low infrared radiation. Fe_3O_4 nanostructure films can be heated to 350 °C under light irradiation, and this system shows effective visible-light-driven ammonia synthesis production of 3677 μg g^{-1} h^{-1} under gas–solid phase catalysis without noble metals.

Ammonia is an essential source for the manufacture of fertilizers, the chemical industry, metallurgy, medicine, explosives and other industries, and is importantly proposed as a hydrogen carrier to replace carbon-based fossil fuels in the future.[1–4] Traditionally, ammonia synthesis has involved the reaction of nitrogen (N_2) and hydrogen (H_2) over iron-based catalysts *via* the Haber–Bosch process. However, the Haber–Bosch process consumes more than 1% of global energy supply and belches out 1.5% of total global CO_2 emissions annually.[5,6] Therefore, it is extremely imperative for human beings to develop sustainable and environmentally-friendly strategies under ambient conditions.

In 1977, the first groundbreaking study on as-synthesized iron-doped TiO_2 photocatalysts for N_2 fixation under UV light was accomplished by Guth and Schrauzer.[7] Since then, a flurry of research has been devoted to the development of photocatalytic N_2 fixation.[8–10] At present solar-thermal energy conversion to trigger thermal catalysis has also attracted attention.[11,12] In the area of solar-thermal energy conversion catalysis, the material is the key to improving the high temperature upon light-irradiation. Hence, it is extremely imperative to design the ideal solar-thermal material with high solar absorption and low thermal emittance.

Among various materials, Fe_3O_4 is a typical solar-thermal material with a narrow band gap that can nearly absorb the full solar spectrum. On the other hand, taking inspiration from nitrogenase enzymes, iron (Fe^-) proteins improve the N≡N activation by proton and electron transfer processes.[13] This shows that Fe-based transition-metal compounds efficiently promote N≡N cleavage, and exhibit low barriers for nitrogen dissociation. Furthermore, it is known that Fe element plays an important role in industrial thermal catalytic ammonia synthesis. Hence, Fe_3O_4 with synergistically intense sunlight absorbance and low thermal conductivity used by solar-thermal catalysis might offer an accessible kinetic pathway toward N_2 and H_2 activation under light radiation.

Herein, we demonstrate that Fe_3O_4 porous microstructures synthesized on stainless steel by an *in situ* hydrothermal method can simultaneously balance solar absorption and thermal emittance, which increase the sunlight irradiation temperature and possess remarkable photocatalytic ammonia synthesis in gas–solid phase catalysis under visible-light spectroscopy due to their high carrier concentration, ultrasmall size and broad spectrum absorption. The catalyst can absorb sunlight in the whole UV-vis-NIR region, where the solar-thermal temperature can raise to above 350 °C and meet the temperature requirement for ammonia synthesis. In addition, Fe_3O_4 films treated with hydrogen exhibit abundant oxygen vacancies, which can promote the effective separation of photogenerated charge carriers, enhance the reduction ability of electrons and be beneficial for efficient nitrogen activation.

The spinel nanoparticle film (denoted as FO) was synthesized *via* a hydrothermal process using fresh stainless steel (SS) and sodium hydroxide (NaOH) as precursors under ambient conditions. The as-prepared films were respectively followed by annealing in a hydrogen atmosphere and oxygen atmosphere for 2 hours at a high temperature, denoted as HFO and OFO. The crystalline phase composition and surface topography of the films before and after annealing under different atmospheres were characterized using X-ray diffraction (XRD) and scanning electron microscopy (SEM). As shown in Fig. 1a, the obvious diffraction peaks (2θ = 43.48°, 50.54°) represent

[a] *School of Chemistry and Chemical Engineering, Shandong Provincial Key Laboratory of Chemical Energy Storage and Novel Cell Technology, Liaocheng University, Liaocheng 252059, P. R. China. E-mail: furong@lcu.edu.cn*
[b] *State Key Laboratory of Inorganic Synthesis and Preparative Chemistry, College of Chemistry, Jilin University, Changchun 130012, P. R. China*
[c] *School of Physics and Electronics, Shandong Normal University, Jinan 250014, P. R. China*

† Electronic supplementary information (ESI) available. See DOI: https://doi.org/10.1039/d4cc04112g

Published on 10 October 2024. Downloaded on 2/13/2026 7:29:37 AM.

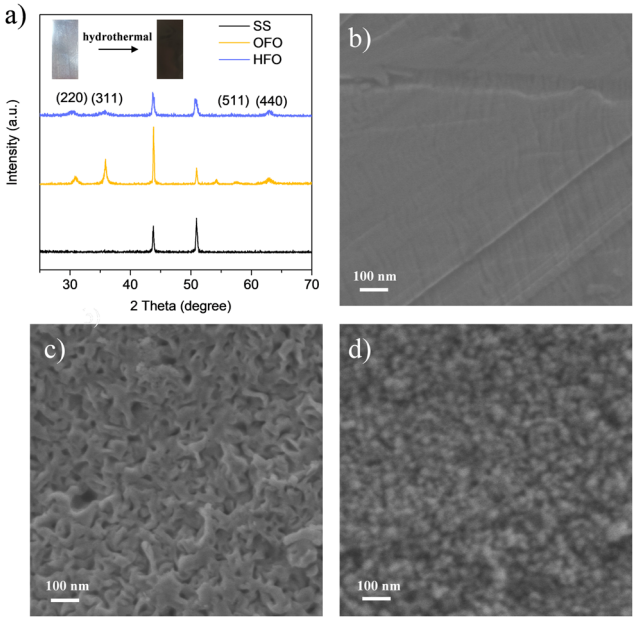

Fig. 1 (a) The XRD patterns of SS, OFO and HFO. (b)–(d) SEM image of SS, OFO and HFO.

stainless steel (SS). It was obviously found that the peaks of the as-synthesized film before annealing treatment were extremely weaker on stainless steel (Fig. S1, ESI†), indicating a poorer crystallinity. After annealing treatment, the other characteristic peaks (2θ= 30.1°, 35.2°, 56.2°, 62.5°) are assigned to their indices ((220), (311), (511), (440)), and are highly consistent with the spinel phase Fe_3O_4 crystals (JCPDS no. 65-3107).[14] Furthermore, the characteristic peaks of HFO film were weaker and wider compared to that of OFO film, where this phenomenon maybe be ascribed to the presence of oxygen vacancies. In addition, it can be seen by their photographs that HFO exhibited a deep black color in the illustration of Fig. 1a. As shown in Fig. 1b and Fig. S2 (ESI†), stainless steels initially feature a smooth and flat surface, but possess a foamed nanostructure consisting of numerous nanoparticles after hydrothermal treatment in concentrated alkali solution on a large scale. During the reaction, some of the metal ions dissociated in the alkali solution causing irregular pores, and the other metal ions are oxidized *in situ* to form spinel on the surface of the stainless steel substrate. Fig. 1c shows the morphology of the films with oxygen annealing treatment under high temperature. It is observed that the nanoparticles grown on stainless steel are seriously agglomerated, resulting in the attenuation of the number of pores to a certain extent and the weakening of the solar selective absorptance. In addition, nanoparticle films after hydrogen annealing treatment are looser and still maintain more interspaces, implying that the possible presence of oxygen vacancies prevents the nanoparticles from agglomerating on the surface and the interspaces between the nanoparticles can ensure better light absorption.

In order to further investigate the microstructure of the resultant films, a small number of nanoparticles were scraped off the surface of the film for TEM analysis by different magnifications. As revealed in Fig. 2a, it is difficult to make even nanoparticles dispersed by ultrasonic treatment over a long time owing to the intrinsic magnetic Fe_3O_4. The TEM image shows the obvious features of nanoparticle stacking morphology. A high-resolution TEM observation by well-defined lattice fringes further confirmed the good crystallization of Fe_3O_4, where the interplanar lattice spacing of 2.06 Å corresponds well to the (222) plane of the spinel structure type of Fe_3O_4 crystals (Fig. 2b). The size of the nanoparticles showing a regular morphology is normally distributed with an average particle size of ~10 nm (Fig. 2c). To ascertain the distribution of Fe element and O element, energy-dispersive X-ray spectroscopy (EDS) mapping on Fe_3O_4 film was performed. Fig. 2d indicates a homogeneous distribution of Fe and O on the catalyst surface at a large scale. From energy-dispersive X-ray spectroscopy (EDS), the concentration of iron ions for the as-prepared selective absorber film is dominant about 43.1%. On account of the fact that it is affected by the electrode potential, the iron element is more likely to be corroded under high temperature and high pressure.

In order to confirm the surface electronic states and the composition of the as-prepared films processed by different conditions, high-resolution X-ray photoelectron spectroscopy (XPS) measurements were executed. As can be seen from Fig. 3a and Fig. S4 (ESI†), the Fe 2p of all films including FO, HFO and OFO were two peaks at 724.9 eV and 711.6 eV with a spin-orbital doublet splitting (Δ, Fe $2p_{1/2}$–Fe $2p_{3/2}$). Therein, the Fe $2p_{1/2}$ XPS spectra can be divided into two peaks at 726.2 eV and 724.6 eV, which are respectively indicated as Fe^{2+} $2p_{1/2}$ and Fe^{3+} $2p_{1/2}$.[15] The Fe $2p_{3/2}$ XPS spectra were divided into two peaks at 714 eV and 711 eV, in line with the characteristic peaks of Fe^{2+} $2p_{3/2}$ and Fe^{3+} $2p_{3/2}$.[16] This manifests that Fe(II) and Fe(III) predominantly existed in the films. Besides, the O 1s spectrum appears to exhibit three prominent peaks at the position of 529.4 eV,

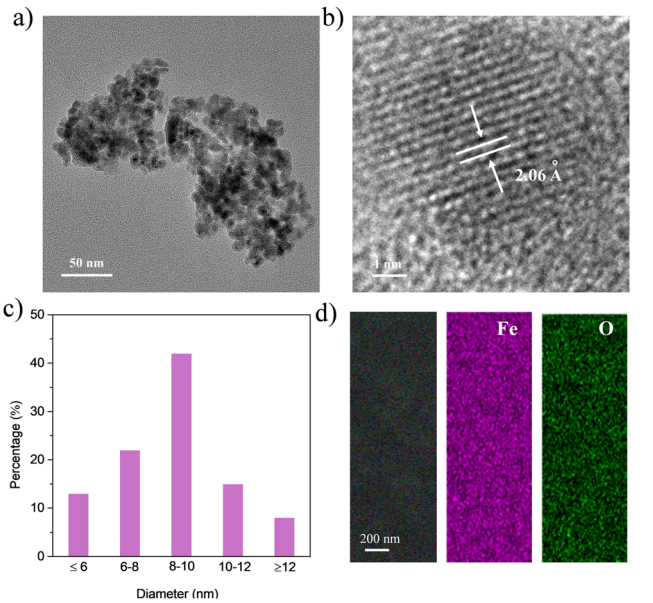

Fig. 2 (a) The TEM patterns of HFO. (b) High-resolution TEM images of HFO. (c) The corresponding particle size distribution. (d) EDS elemental mapping profiles of HFO for Fe (purple), and oxygen (green).

 This journal is © The Royal Society of Chemistry 2024

Published on 10 October 2024. Downloaded on 2/13/2026 7:29:37 AM.

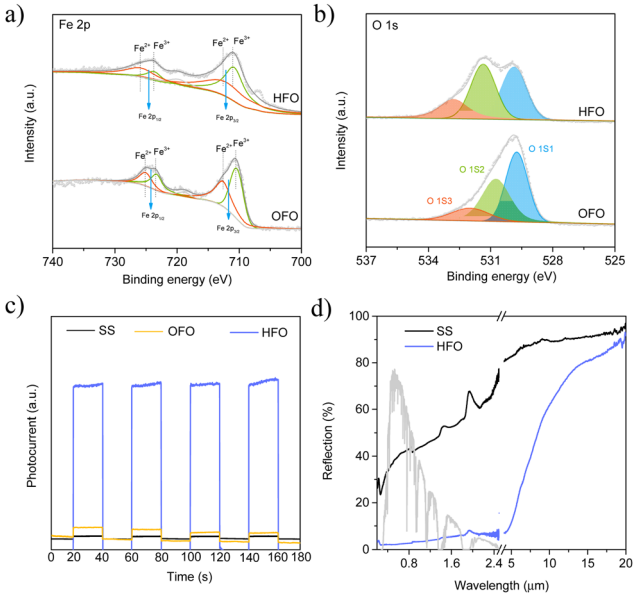

Fig. 3 (a) XPS spectra of the Fe 2p peaks for OFO and HFO. (b) XPS spectra of the O 1s peaks for OFO and HFO, (c) the photocurrent responses of SS, OFO and HFO. (d) UV-vis reflectance spectra and IR reflectance spectra of SS and HFO.

531.2 eV and 532.8 eV, which may respectively correspond to the lattice oxygen, oxygen vacancies and surface-adsorbed hydroxyl groups.[17,18] On the basis of the fitted O 1s XPS spectra (Fig. 2b), the ratio of the oxygen vacancy (O_V) obviously occupies about 49.9% after the hydrogen heat treatment (Table S1, ESI†). Nevertheless, the oxygen defect content of the films after oxygen annealing treatment is greatly reduced to 39.1%. The increase of oxygen vacancy contributes to high electron density, where anti-bonding π^* orbitals of nitrogen can accept electrons from the catalyst. That can be beneficial to the ammonia synthesis process. The photoluminescence (PL) emission spectra are useful to confirm radiative relaxation in the form of emitted photons. As shown in Fig. S6 (ESI†), OFO films show much stronger light emission in the range from 350 nm to 600 nm than HFO films, indicating that the existence of oxygen vacancies further can inhibit the radiative relaxation of the emitted photon and reduce energy loss, which increases the system temperature. Furthermore, photoelectrochemistry tests are performed (Fig. 3c). It is obviously found that the photocurrent response of HFO films reveals a stronger photocurrent under several on/off irradiation cycles with the stability and repeatability compared to the stainless steel substrate and OFO films. High photocurrent illustrates the more generation of electron–hole pairs. The presence of abundant oxygen vacancies promotes the effective separation of photogenerated charge carriers. This result is consistent with the photoluminescence. In addition, the introduction of oxygen vacancies can act as electron trapping centers and nitrogen active sites, which can accumulate the donation ability of the photogenerated electrons. Based on the investigations above, the general benchmark for the process is proposed. Fe_3O_4 serves as the typical solar-thermal material with a narrow band gap and can produce electron–holes under light irradiation. Then, there are two photoexcited electron transfer pathways in photocatalytic nitrogen fixation. The first pathway is that the photoelectron–holes are in the form of emitted photons to produce radiative relaxation, which elevated the system temperature. The second way mainly is that the photoelectrons transfer from the active sites to adsorbed nitrogen and serve as the electron trapping center for nitrogen by importing highly efficient electrons.

According to UV-vis diffuse absorbance spectra (UV-DRS) (Fig. S7, ESI†), HFO films show a narrow band gap regarded as a typical solar-thermal material, which can almost absorb the entire solar spectrum. Therefore, the type of narrow band gap material can be thermalized by absorbed sunlight *via* electron–electron and electron–phonon scattering. In order to reveal more intuitively the solar absorptance and thermal emittance, the reflection spectra of the spinel films are shown in Fig. 3d. Calculated by formula (1) and formula (2), HFO has the solar absorptance of 95%, and the thermal emittance is correspondingly 33%.[19] HFO is composed of dispersed nanoparticles and more irregular nanopores, where the photons can effectively be trapped by multi-reflection in the interior spaces of the nanostructure. In addition, the nanoparticles with small size are far smaller than the IR wavelength, and thus the absorptance of HFO spinel films in the IR range is weaker along with lower thermal emission. With the extension of the Xe light time, the surface temperature of the film also increases to 350 °C. This phenomenon confirms that narrow-band gap transition metal oxides with nanoparticles and nanopores have low IR radiation, while retaining the superior light absorption to realize a high temperature under vacuum (Fig. 4a).

A series of photocatalytic ammonia synthesis experiments have been studied by a vacuum system under visible and infrared light from a 300 W Xe lamp with different spinel film. Generally, 1 cm × 1 cm of films were placed in the bottom of the quartz reactor under vacuum, injecting the mixture of hydrogen (75%) and nitrogen (25%). In order to eliminate the influence of *N*-impurities, the nitrogen was purified by sulfuric acid and distilled water. The resulting ammonia was detected by ion chromatography and spectroscopy.[20] Various FO films with different concentrations of alkalinity solution were prepared. Fig. S10 (ESI†) shows that HFO synthesized with 12 M sodium hydroxide had the highest photocatalytic performance for nitrogen fixation. Hence, HFO films with 12 M sodium hydroxide in a hydrothermal environment were chosen as the heat treatment object. Then, the current is adjusted to assess photocatalytic performance. Fig. S11 (ESI†) shows that the performance is the highest when the current is 15 A. As revealed in Fig. 4b, the optimized HFO films display excellent activity for ammonia synthesis. A splendid NH_3 generation rate of 3677 $\mu g\ h^{-1}\ g^{-1}$ was achieved under light irradiation, which was higher than that of OFO films. HFO is one of the most efficient photocatalysts for gas–solid phase ammonia synthesis without noble metals. It is unambiguously confirmed that the abundant OVs make an important contribution for efficient photocatalytic nitrogen fixation.

As shown in Fig. 4c, the HFO films exhibited outstanding photocatalytic activity during the whole wavelength range from 200 nm to 1000 nm. More interestingly, it is obvious that

Published on 10 October 2024. Downloaded on 2/13/2026 7:29:37 AM.

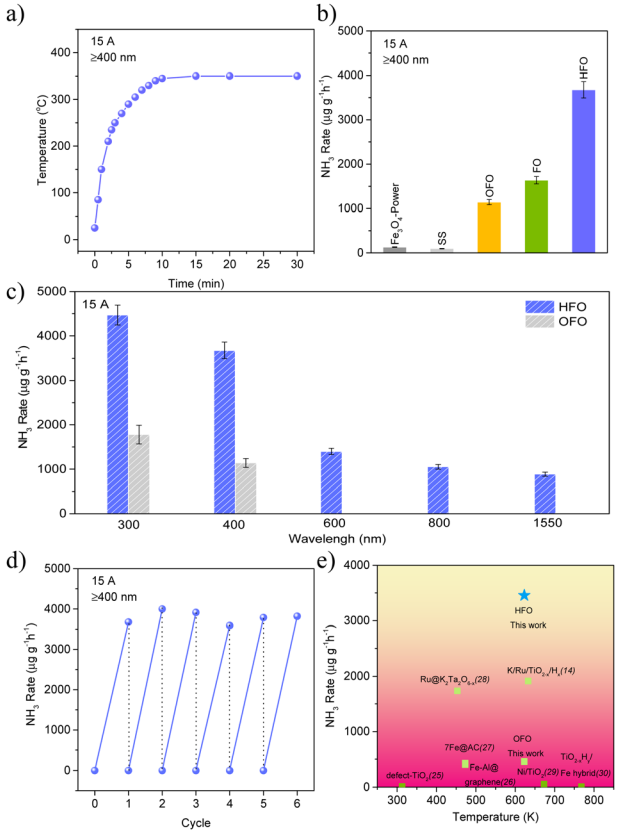

Fig. 4 (a) Time-dependence of temperature for HFO. (b) Photocatalytic ammonia production rates of various catalysts. (c) Wavelength dependence of the ammonia synthesis rate for OFO and HFO. (d) Cycling test for HFO. (e) Summary of ammonia synthesis rate achieved in this work and other representative photothermal catalysts.

highlighted activity was obtained for the HFO films under 1550 nm infrared light irradiation. Considering that HFO films have a narrow band, the key to the infrared performance is ratiocinated to be in connection with solar absorptance, which enabled the generation of hot electrons. Furthermore, the HFO film was used for multiple photocatalytic ammonia synthesis reactions to research the cyclability and stability of the film. Particularly noted, the photocatalytic activity of the films well remains stable during six cycling tests without significant attenuation, and both the crystal structure and morphology of the Fe_3O_4 nanostructure films remained the same after cyclic tests as shown in Fig. S13 (ESI†), signifying that the resulting HFO films possess superior stability and reusability (Fig. 4d). As observed in Fig. 4e, calculated per unit mass of catalyst, HFO shows excellent performance. In addition, a mechanism process is shown in Fig. S14 (ESI†).

In summary, we established an efficient solar-thermal conversion system, in which the black solar-thermal material (Fe_3O_4 films) with high solar absorption and low infrared radiation significantly elevates solar heating temperatures. A record-breaking visible-light-driven ammonia synthesis was realized through this innovative system. In addition, high carrier concentration, broad spectrum absorption and high reduction ability synergistically enhance the nitrogen activation of Fe_3O_4 films. This work provides new insights for designing solar-thermal catalysts for gas–solid phase photocatalytic ammonia synthesis.

This work was funded by the National Natural Science Foundation (NSFC) of China (grant no. 22309071, 12204286), the Natural Science Foundation of Shandong Province (grant no. ZR202111300197), the Doctoral Program of Liaocheng University (grant no. 318052145), the Development Program of Youth Innovation Team in Colleges and Universities of Shandong Province (grant no. 2022KJ109), and the Guangyue Young Scholar Innovation Team of Liaocheng University (grant no. LCUGYTD2022-02).

Data availability

The data supporting this article have been included as part of the ESI.†

Conflicts of interest

There are no conflicts to declare.

Notes and references

1 C. J. Van der Ham, M. T. Koper and D. G. Hetterscheid, *Chem. Soc. Rev.*, 2014, **43**, 5183.
2 S. J. Leghari, N. A. Wahocho, G. M. Laghari, A. HafeezLaghari, G. MustafaBhabhan, K. HussainTalpur, T. A. Bhutto, S. A. Wahocho and A. A. Lashari, *Adv. Environ. Biol.*, 2016, **10**, 209.
3 S. L. Foster, S. I. P. Bakovic, R. D. Duda, S. Maheshwari, R. D. Milton, S. D. Minteer, M. J. Janik, J. N. Renner and L. F. Greenlee, *Nat. Catal.*, 2018, **1**, 490.
4 G. F. Chen, X. R. Cao, S. Q. Wu, X. Y. Zeng, L. X. Ding, M. Zhu and H. H. Wang, *J. Am. Chem. Soc.*, 2017, **139**, 9771.
5 H.-P. Jia and E. A. Quadrelli, *Chem. Soc. Rev.*, 2014, **43**, 547.
6 J. Lee, L. L. Tan and S. P. Chai, *Nanoscale*, 2021, **13**, 7011.
7 G. N. Schrauzer and T. D. Guth, *J. Am. Chem. Soc.*, 1977, **99**, 7189.
8 Z. Li, Z. Y. Gao, B. W. Li, L. L. Zhang, R. Fu, Y. Li, X. Y. Mu and L. Li, *Appl. Catal., B*, 2020, **262**, 118276.
9 G. X. Song, R. Gao, Z. Zhao, Y. J. Zhang, H. Q. Tan, H. B. Li, D. D. Wang, Z. C. Sun and M. Feng, *Appl. Catal., B*, 2022, **301**, 120809.
10 R. Fu, Y. Wang, G. M. Wang, Q. Y. Zhan, L. L. Zhang and L. Liu, *Green Chem.*, 2023, **25**, 8531.
11 C. L. Mao, L. H. Yu, J. Li, J. C. Zhao and L. Z. Zhang, *Appl. Catal., B*, 2018, **224**, 612.
12 X. N. Bian, Y. X. Zhao, G. I. N. Waterhouse, Y. X. Miao, C. Zhou, L.-Z. Wu and T. R. Zhang, *Angew. Chem., Int. Ed.*, 2023, **62**, e202304452.
13 K. M. Lancaster, M. Roemelt, P. Ettenhuber, Y. Hu, M. W. Ribbe, F. Neese, U. Bergmann and S. DeBeer, *Science*, 2011, **334**, 974.
14 R. Fu, X. F. Wu, X. L. Wang, W. Ma, L. Yuan, L. Gao, K. K. Huang and S. H. Feng, *Appl. Surf. Sci.*, 2018, **458**, 629.
15 S. Tiwari, R. Prakash, R. J. Choudhary and D. M. Phase, *J. Phys. D: Appl. Phys.*, 2007, **40**, 4943.
16 G. K. Reddy, P. Boolchand and P. G. Smirniotis, *J. Phys. Chem. C*, 2012, **116**, 11019.
17 X. Xiong, Y. Wang, J. P. Ma, Y. X. He, J. Y. Huang, Y. J. Feng, C. G. Ban, L.-Y. Gan and X. Y. Zhou, *Appl. Surf. Sci.*, 2023, **616**, 156556.
18 X. Y. Hu, J. T. Wang, J. Wang, Y. Deng, H. D. Zhang, T. Xu and W. L. Wang, *Appl. Catal., B*, 2022, **318**, 612.
19 H. Wang and L. P. Wang, *Opt. Express*, 2013, **21**, A1078.
20 Y. X. Zhao, R. Shi, X. N. Bian, C. Zhou, Y. F. Zhao, S. Zhang, F. Wu, G. I. N. Waterhouse, L. Z. Wu, C. H. Tung and T. R. Zhang, *Adv. Sci.*, 2019, **6**, 1802109.

 This journal is © The Royal Society of Chemistry 2024